Discovery of High-Entropy Oxide Electrocatalysts: From Thin-Film Material Libraries to Particles

Valerie Strotkötter,[||] Olga A. Krysiak,[||] Jian Zhang, Xiao Wang, Ellen Suhr, Wolfgang Schuhmann, and Alfred Ludwig*
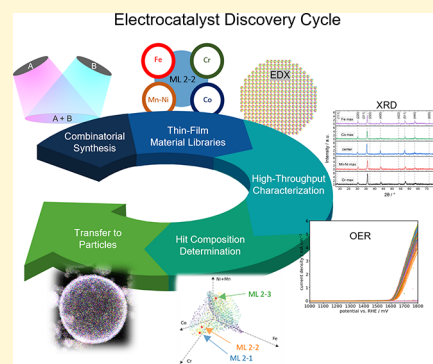
Read Online

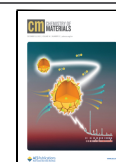ACCESS | 📊 Metrics & More | 📰 Article Recommendations | 🆂🅸 Supporting Information

ABSTRACT: Discovery of new high-entropy electrocatalysts requires testing of hundreds to thousands of possible compositions, which can be addressed most efficiently by high-throughput experimentation on thin-film material libraries. Since the conditions for high-throughput measurements ("screening") differ from more standardized methods, it is frequently a concern whether the findings from screening can be transferred to the commonly used particulate catalysts. We demonstrate the successful transfer of results from thin-film material libraries to particles of Cantor alloy oxide $(Co\text{-}Cr\text{-}Fe\text{-}Mn\text{-}Ni)_3O_4$. The chemical compositions of the libraries, all single-phase spinels, cover a wide compositional range of $(Cr_{8.1-28.0}Mn_{11.6-28.4}Fe_{10.6-39.0}Co_{11.4-36.7}Ni_{13.5-31.4})_{37.7\pm0.6}O_{62.3\pm0.6}$, with composition-dependent lattice constant values ranging from 0.826 to 0.851 nm. Electrochemical screening of the libraries for the oxygen evolution reaction (OER) identifies $(Cr_{24.6\pm1.4}Mn_{15.7\pm2.0}Fe_{16.9\pm1.8}Co_{26.1\pm1.9}Ni_{16.6\pm1.7})_{37.8\pm0.8}O_{62.2\pm1.2}$ as the most active composition, exhibiting an overpotential of 0.36 V at a current density of 1 mA cm^{-2}. This "hit" in the library was subsequently synthesized in the form of particles with the same composition and crystal structure using an aerosol-based synthesis strategy. The similar OER activity of the most active thin-film composition and the derived catalyst particles validates the proposed approach of accelerated discovery of novel catalysts by screening of thin-film libraries.

INTRODUCTION

The search for new catalysts is of great interest as they are essential for new energy-efficient, cost-effective, and, most importantly, climate-neutral industrial processes. In this regard, great efforts are being made to replace the widely used precious metal catalysts with more abundant and cheaper materials.[1,2] One of the most relevant reactions for which noble metal catalysts are commonly used is the oxygen evolution reaction (OER).[3] Owing to its sluggish four-electron process, it is considered as the crucial limiting half-reaction of water splitting technologies, and thus, developing high-performance OER electrocatalysts is vital to improving the overall efficiency of this process.[4] Electrocatalysts based on transition metals and oxides are extensively studied as possible alternatives to precious metal catalysts, since these elements are widely available, inexpensive, and highly active.[5−9] Out of this group, OER catalysts in the form of spinel-type oxides have attracted significant attention as it is possible to tailor their properties by changing the metal cations and their ratios.[10−15]

Recently a new class of materials for catalytic applications emerged — the so-called high-entropy materials (HEMs).[16−22] HEMs consist of at least five different elements, which are randomly distributed in one homogeneous single phase. The first reported HEMs were high-entropy alloys (HEAs), including the so-called Cantor alloy CrMnFeCoNi.[23,24] Later, the concept of HEM was extended to other multicomponent systems: high-entropy oxides (HEOs),[25] nitrides,[26,27] phosphides,[28] carbides,[29] fluorides,[30,31] sulfides,[32,33] borides,[34,35] silicides,[36] hydroxides,[37] or metal-organic frameworks,[38] which provide promising properties for catalytic applications, energy storage, thermal and environmental protection, or thermo-electricity.

Here, we report the synthesis, properties, and characterization of a high-entropy spinel oxide OER electrocatalyst. Searching for novel HEM electrocatalysts is a demanding multidimensional challenge. Considering the nonradioactive and not extremely toxic elements from the periodic table that might be used in a sustainable way, there are about 50 elements to choose from. This results in more than 2 million possible five-element material systems, where the electrochemical activity can possibly change by a factor of 10 or more depending on the ratio of elements.[39−41] Since no theoretical

model currently exists that can reliably predict the electrochemical activity of HEMs, the synthesis and testing of a huge number of element compositions is inevitable.[42] Conventional one-by-one experimentation cannot accomplish this efficiently, which makes the use of high-throughput methods of crucial importance.[43] Combinatorial synthesis of HEM libraries and their electrochemical screening with scanning droplet cells has been shown to efficiently cover large composition ranges of HEA systems, and active compositions and compositional activity trends can be rapidly and reliably identified in the polyelemental search space.[19,40] Combining theory, simulation, and machine learning with high-throughput experimentation can enable the prediction and understanding of new HEMs.[39,44,45]

However, an important issue is to transfer the hit compositions of the high-throughput electrochemical screening to conditions closer to industrial applications. The first step in this process would be moving from the high-throughput characterization of thin films to well-defined and accepted electrocatalyst characterization strategies like rotating disk electrode measurements, which was done in this contribution. We demonstrate that thin-film screening results can be transferred reliably to particulate catalysts confirming the compatibility of high-throughput screening of thin films with existing electrochemical techniques.

We synthesized HEO thin films and particles based on the well-known Cantor alloy, which were tested for their properties as OER electrocatalysts. The obtained materials were single-phase spinels in the "Cantor alloy oxide" system (Cr-Mn-Fe-Co-Ni)$_3$O$_4$.

To investigate the Cantor alloy oxide system over large compositional ranges, we used thin-film material libraries (MLs), which were fabricated by combinatorial sputter deposition on 100 mm diameter thermally oxidized Si wafer substrates.[43] Preparing samples by cosputtering from multiple sources in the form of MLs with continuous composition gradients enables the investigation of much larger parts of the composition space of the studied material system compared to the synthesis of individual samples, i.e., one composition vs several hundred produced in one experiment. However, analysis of only one ML of a compositionally complex system is not sufficient to get clear information about activity trends and interaction of particular elements as the composition gradients of elements deposited from neighboring and opposing targets are correlated. Namely, gradients of elements deposited from opposing targets are reversed, when the amount of one element is increasing, and the other is decreasing. For neighboring targets, the gradient direction is similar but differs by the angle between the targets, and hence the contributions of both elements increase and decrease simultaneously. This problem can be solved by a recently introduced permutation method,[42] i.e., by preparing a set of MLs where the position of the sputter targets is changed for each ML deposition process (see Figure 1). For example, during the preparation of ML 2-1, Fe and Cr, Cr and Co, Co and Mn-Ni, and Mn-Ni and Fe were placed next to each other (target position clockwise from upper left: Fe, Cr, Co, and Mn-Ni), with Fe and Co and Cr and Mn−Ni opposite to each other. For ML 2-2, the positions of Cr and Co were switched (target position clockwise from upper left: Fe, Co, Cr, Mn-Ni), changing both opposing target pairs and three out of four neighboring targets. Similarly, for the synthesis of ML 2-3, the positions of Fe and Co were switched from the positions for
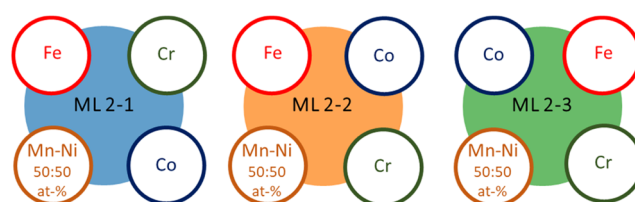
Figure 1. Schematic of the permutated target arrangements for the combinatorial synthesis of HEO thin-film material libraries (MLs) by reactive cosputtering from four targets using a target permutation approach. The positions of the targets for each permutation for the synthesis of the libraries ML 2-1, ML 2-2, and ML 2-3 are indicated.

the synthesis of ML 2-2. Thanks to this, we obtain all possible combinations of target positions, which allows us to disentangle correlated gradients and get more insight into the contribution of particular elements to the material properties.

The crystal structure and lattice constants of the thin films were determined by X-ray diffraction (XRD), their chemical composition by energy-dispersive X-ray spectroscopy (EDX), and the near-surface composition by X-ray photoelectron spectroscopy (XPS). Furthermore, their microstructure was characterized by scanning electron microscopy (SEM) and atomic force microscopy (AFM), and their electrical resistance was determined by four-point probe measurements. The electrochemical properties, i.e., OER activity, of the oxide films were measured using the high-throughput method with a scanning droplet cell (SDC). The identified most active hit composition was then synthesized in the form of particles. Their electrochemical activity toward OER was measured in a rotating disk electrode setup.

■ EXPERIMENTAL SECTION

Synthesis of (Cr-Mn-Fe-Co-Ni)$_3$O$_4$ MLs. The MLs were fabricated by reactive codeposition in a four-cathode sputter system (ATC 2200, AJA International). Three elemental targets and one alloy sputter target (diameter 100 mm) were used: Co: 99.99 atom %, Cr: 99.95 atom %, Fe: 99.99 atom %, and Mn$_{50}$Ni$_{50}$: 99.95 atom %. The cathode angle was 27.5° to the substrate normal, and the distance between the target and the substrate was 140 mm. This leads to well-controlled continuous composition spreads (i.e., composition gradients) of all five elements on the substrate.

For all deposition processes, the following process parameters were used: 37 W DC power for Co, 155 W DC power for Cr, 222 W RF power for Fe, 67 W pulsed DC power (frequency 10 kHz, pulse length 5 μs) for Mn-Ni , an Ar/O$_2$ flow rate of 80/40 sccm, and a deposition process pressure of 0.4 Pa. The target arrangements were varied to obtain three different setup-possible permutations (see Figure 1), different deposition temperatures (573, 773, 973 K), and different sputtering times to adjust the film thickness.

To be able to analyze the MLs with different analysis methods, each ML was deposited on two different substrates. For the XRD and resistivity analyses, 500 nm thin films were deposited on 100 mm diameter Si wafers with a 500 nm thick SiO$_2$ layer acting as a diffusion barrier. For the SDC analyses, the investigated ML was nominally 50 nm thick and was deposited on a previously sputtered 50 nm Pt electrode layer on a 10 nm Ta adhesion layer also on a 100 mm diameter Si/SiO$_2$ wafer. Commonly used Ti was not used as the adhesion layer because it is unstable at high-temperature deposition processes with reactive O$_2$ plasma.[34,35] The process parameters for this prior deposition were 100 W DC power for both Ta and Pt, sputtered from elemental targets (99.99 atom %), a process pressure of 0.13 Pa, and a flux of 40 sccm Ar. The process was carried out at room temperature.
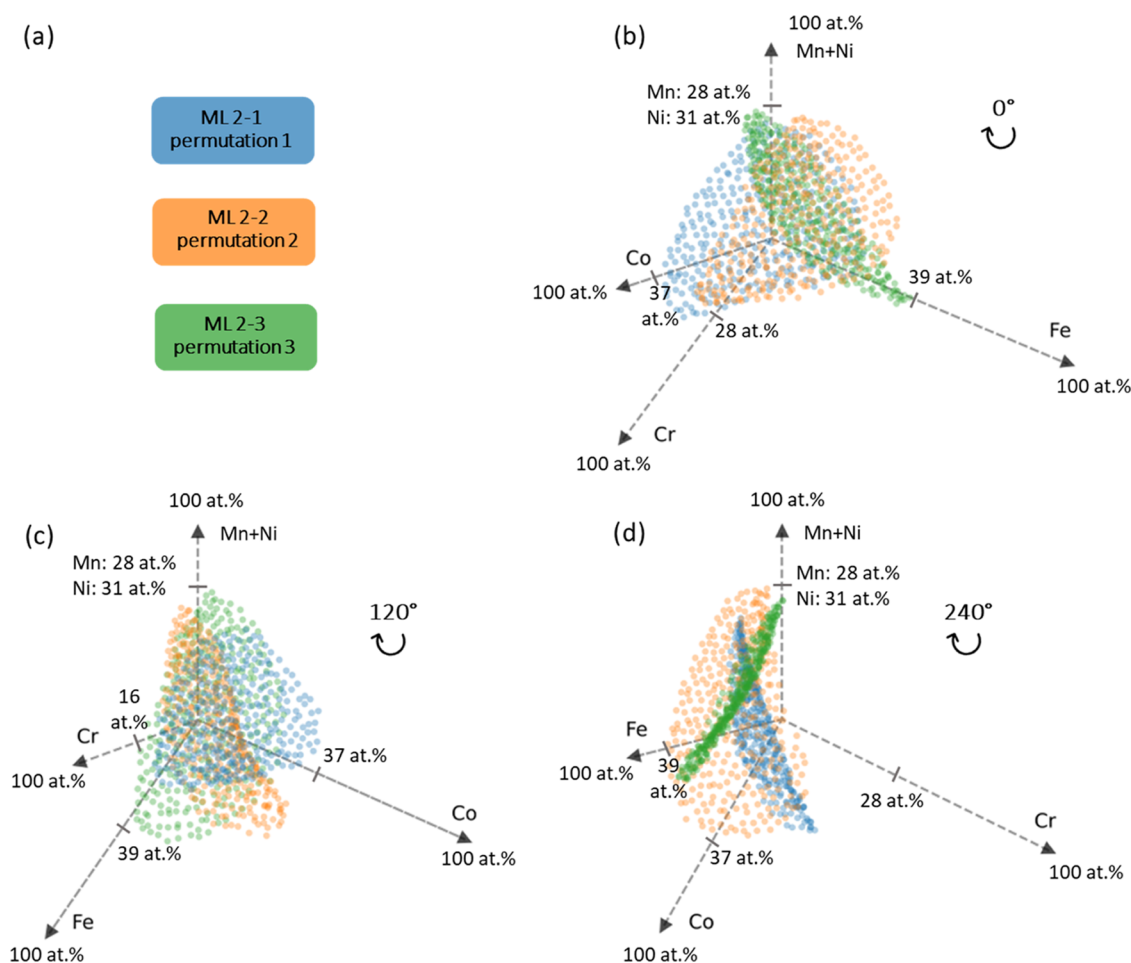
Figure 2. Barycentric tetrahedron representation of the covered composition space, (a) color code of the MLs. (b−d) 3D visualization of the five-dimensional metal composition space in three viewing directions (blue points: initial target arrangement - permutation 1, orange and green points: permutated target arrangements, permutations 2 and 3, respectively).

Chemical and Structural Characterization. For the chemical and structural analysis, the MLs were divided into 342 measurement areas (MA) with a spacing of 4.5 mm in the x- and y-directions. The analyses with EDX, XRD, and SDC were performed in an automated way using high-throughput setups, allowing reliable measurements of previously defined MAs. EDX high-throughput mappings were performed using a scanning electron microscope (JEOL 5800) with an INCA X-act detector (Oxford Instruments). The acceleration voltage was 20 kV, and the magnification was 600×. The measurement accuracy was about 1 atom %. For the high-throughput XRD measurements, a Bruker D8 Discover from Bruker Corporation in Bragg-Brentano geometry was utilized. It was equipped with a VANTEC-500 area detector and a Cu Kα radiation source. The sample-to-detector distance was 14.9 mm. The X-ray beam size was adjusted to 1 mm, with a collimator diameter of 1 mm and a divergence below 0.007°. The peak layer accuracy of the instrument was ±0.02 2θ°. For each MA, four frames were recorded. They were transformed into one-dimensional (1D) diffractograms using the software DIFFRAC.EVA from Bruker Corporation. The surface composition analysis of the MLs was carried out via an X-ray photoelectron spectroscope (Kratos Axis Nova, U.K.) using monochromatic Al Kα radiation (1486.6 eV/300 W) as the excitation source. Quantification and peak fitting of the different components in the XPS spectra were performed using the software ESCApe (Kratos, U.K.). The Shirley algorithm was used for background subtraction. SEM images were recorded using a JEOL JSM-7200F operating at a working distance of 10 nm and with an accelerating voltage of 10 kV. Atomic force microscopy (AFM) measurements were performed with a Bruker FastScan scanning probe microscope in PeakForce Tapping

mode with ScanAsyst using a FastScan A probe (spring constant ca 18 Nm^{-1}). Powder XRD measurements were performed using a Bruker D8 Discover X-ray diffractometer with a Cu Kα radiation source (λ = 0.15418 nm) in the range 2θ = 15 to 90°. TEM, scanning TEM (STEM), and HR-TEM images were obtained using a JEOL microscope (JEM-2800) with a Schottky-type emission source working at 200 kV. EDX of the particles was performed using double Si drift detectors (SDD) with a solid angle of 0.98 steradians with a detection area of 100 mm^2.

Aerosol-Based Particle Synthesis. A metal salt precursor solution (metal nitrates, Sigma Aldrich) containing the desired ratio of metals was prepared in ethanol and sprayed onto a deflector plate to form aerosols. Aerosol drops were transported through a tube immersed in a tube furnace. The furnace was heated to 1073 K, causing the evaporation of the solvent and allowing the collection of the dried particles on the ashless filter papers located after the furnace. Next, we used a method known from gravimetric analysis (volatilization) to remove residues of the precursor solution and convert all of the carbon from the filter paper into CO_2. This was obtained by heating the filter paper with the collected particles in the flow of oxygen until the paper burned. After that, the catalyst particles were annealed at 773 K in the flow of oxygen to form the desired oxide.

Electrochemical Characterization. All electrochemical measurements of the thin-film samples were done using the scanning droplet cell (SDC) technique, allowing site-localized characterization. The measurements were conducted in 0.05 M KOH electrolyte in a three-electrode system containing a Pt wire and a Ag|AgCl|3M KCl as counter and reference electrodes, respectively. Linear sweep
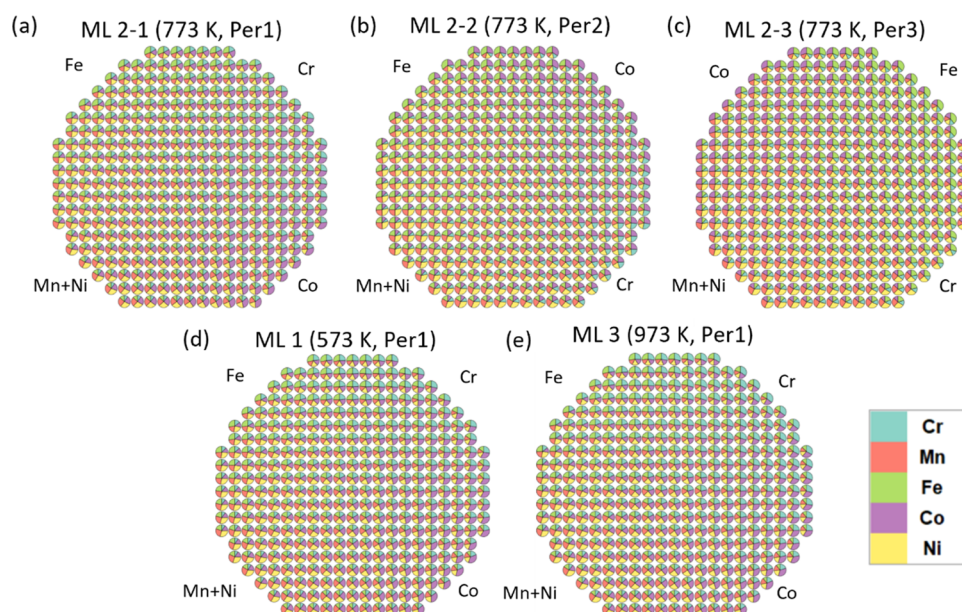
Figure 3. Visualization of the distribution of chemical compositions over the MLs. Each pie chart shows the composition of one measurement area. Data for three permutations deposited at 773 K are shown in panels (a−c): (a) ML 2-1, (b) ML 2-2, and (c) 2-3. The chemical composition of samples prepared at 573 K (ML 1) and 773 K (ML 3) are presented in panels (d, e), respectively. Cathode positions during the deposition process are marked in the figure.

voltammograms (LSVs) for the OER were recorded between 1 and 1.8 V vs the reversible hydrogen electrode (RHE) with a scan rate of 10 mV s^{-1}. All potentials in the manuscript are reported versus the RHE and were calculated using the following equation

$$U_{RHE} = U_{(Ag|AgCl||3M\ KCl)} + 0.210 + (0.059 \cdot pH)$$

where $U_{(Ag|AgCl||3\ M\ KCl)}$ is the potential measured vs the Ag|AgCl||3M KCl reference electrode, 0.210 V is the standard potential of the Ag|AgCl||3M KCl reference electrode at 298 K. 0.059 is the result of $(RT) \cdot (nF)^{-1}$, where R is the gas constant, T is the temperature (298 K), F is the Faraday constant, and n is the number of electrons transferred during the reaction.

Electrochemical measurements on powder catalysts were conducted using a rotating disk electrode setup, including a rotator RDE80983 and a potentiostat/galvanostat Autolab PGSTAT 204 (Metrohm). As a working electrode, glassy carbon RDEs modified with the catalyst suspension with a geometric area of 0.113 cm^2 were used. The electrodes were polished before use with different roughness of sandpaper (3, 1, 0.3 μm) and rinsed with distilled water. A Ag/AgCl/KCl (3M) electrode with double junction (1 M KOH) was used as a reference, and a Pt mesh was used as a counter electrode. A ceramic frit filled with pure electrolyte was used to separate the counter electrode from the bulk solution. For the electrode modification, 5 mg/mL of the catalyst suspension consisting of 2 vol % Nafion and equal volume parts of deionized water and ethanol (2:49:49) was sonicated with a tip sonicator (Bandelin Sonopuls UW 3100) for 1 min (amplitude 25%, pulse duration 1s) prior to use. To provide sufficient conductivity of catalyst ink prepared with oxidized particles, carbon black XPB 538 (Orion Engineered Carbons) was added to the suspension. The prepared suspension (4.8 μL) was drop-cast onto the polished working electrode surface, aiming for a catalyst loading of approximately 210 μg cm^{-2}, and left to dry in air prior to measuring for at least 20 min. On each electrode, a conditioning procedure, potential cycling between 0 and 0.4 V vs Ag|AgCl|KCl (3M) at 100 mV s^{-1} for 10 cycles, followed by cyclic voltammetry measurements from 0 to 0.7 V vs Ag|AgCl|KCl (3M) at 10 mV s^{-1} for 3 cycles was conducted in 1 M KOH solution purged with Ar. The RDE rotator speed during conditioning and voltammetry measurements was kept constant at 1600 rpm. All RDE measurements were repeated at least three times

to ensure reproducibility (the average of the measurements is shown in the manuscript). To determine the uncompensated solution resistance, electrochemical impedance spectra (EIS) were recorded after CV measurements at the open-circuit potential in a frequency range between 100 kHz and 10 Hz and an AC amplitude of 10 mV root mean squared (RMS) with no electrode rotation.

Data Analysis. The data analysis and presentation of the composition space were performed in Python 3.9.10.

RESULTS AND DISCUSSION

High-Throughput Experimentation. We started with finding the best ML synthesis temperature for the highest electrochemical activity and then proceeded from this point to extend the composition space by sputtering two additional ML permutations (Figures 2 and S1−S2, SI). The first prepared MLs 1, 2-1, and 3 were sputtered at 573, 773, and 973 K, respectively, with the target arrangement of permutation 1 (see Figure 1). From those MLs, ML 2-1 showed the highest electrochemical activity for compositions containing significant amounts of Cr, Co, and Fe (approx. 20−25 atom %, Figures 3 and S2b, S11, SI). Therefore, 773 K was chosen as the deposition temperature for ML permutations 2 and 3, resulting in ML 2-2 and ML 2-3. Since different thin-film properties are required for different high-throughput measurements, two different thin films, A and B, were prepared for each ML: (A) 500 nm for XRD and EDX, where a thicker film results in fewer substrate signals and higher diffraction intensities and (B) 50 nm on a Pt electrode layer for SDC measurements, which require a sufficient film conductivity. For (B), XPS, SEM, and AFM measurements were also carried out. The synthesis conditions are otherwise the same, so A and B are combined under the appropriate ML notation in further discussion unless it is explicitly noted.

Additionally, to unravel correlated composition gradients, the proposed permutation method enables us to expand the covered composition space to more than 1000 different compositions. A scheme of the cosputter synthesis strategy of
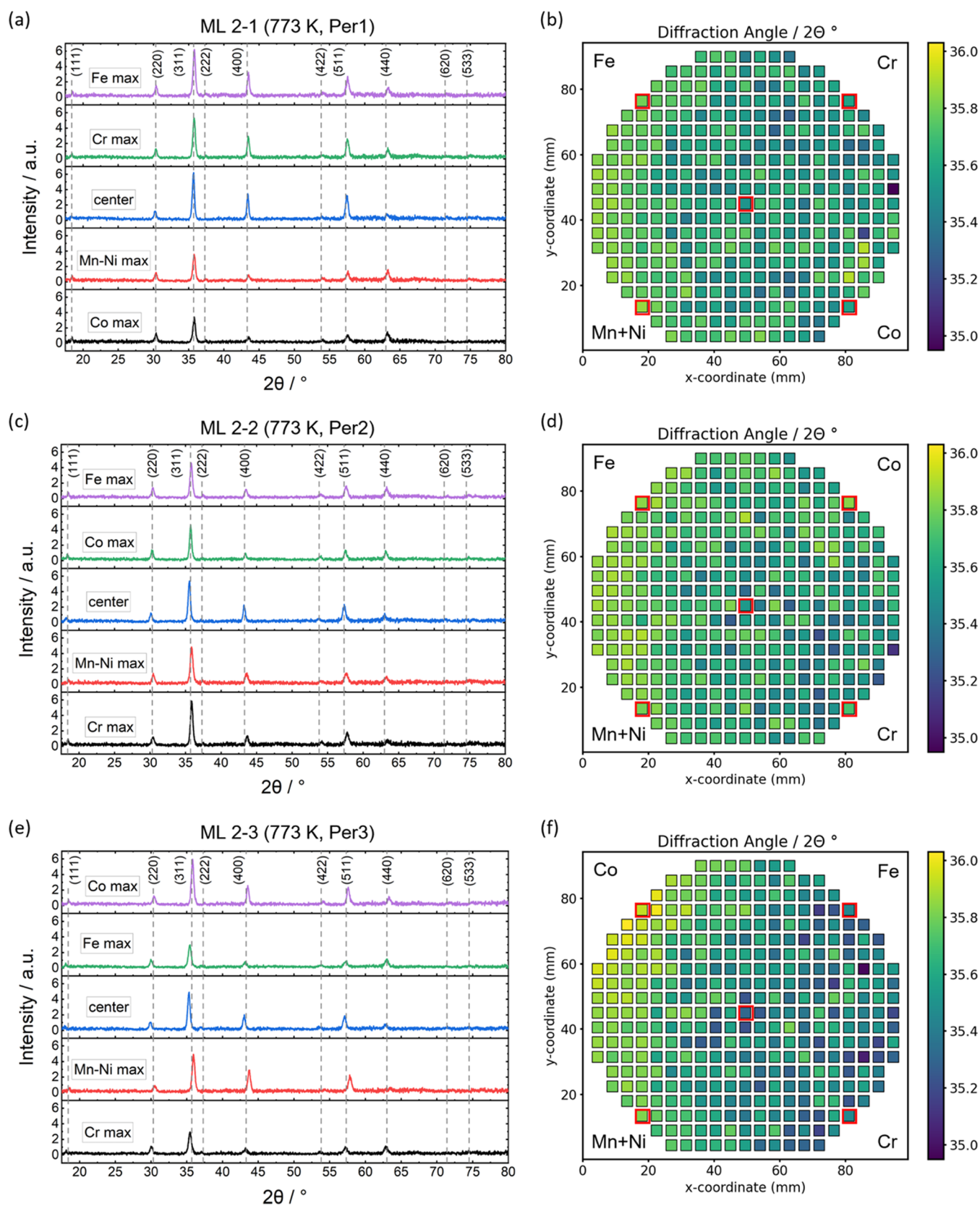
Figure 4. Phase analysis of the HEO libraries: Panels (a, c, and e) show exemplary XRD patterns of the ML permutations deposited at 773 K (ML 2-1, 2-2, and 2-3) for MAs at the center position and closest to the corresponding cathodes (marked with red squares). Reference lines are from Wang et al.[55] Panels (b, d, and f) show the corresponding color-coded (311) diffraction angle maps.

the permutated MLs and a barycentric quaternary representation of the covered composition space are shown in Figures 1

and 2. Each ML creates a curved plane of the covered composition, visualized as a cut through the 3D composition
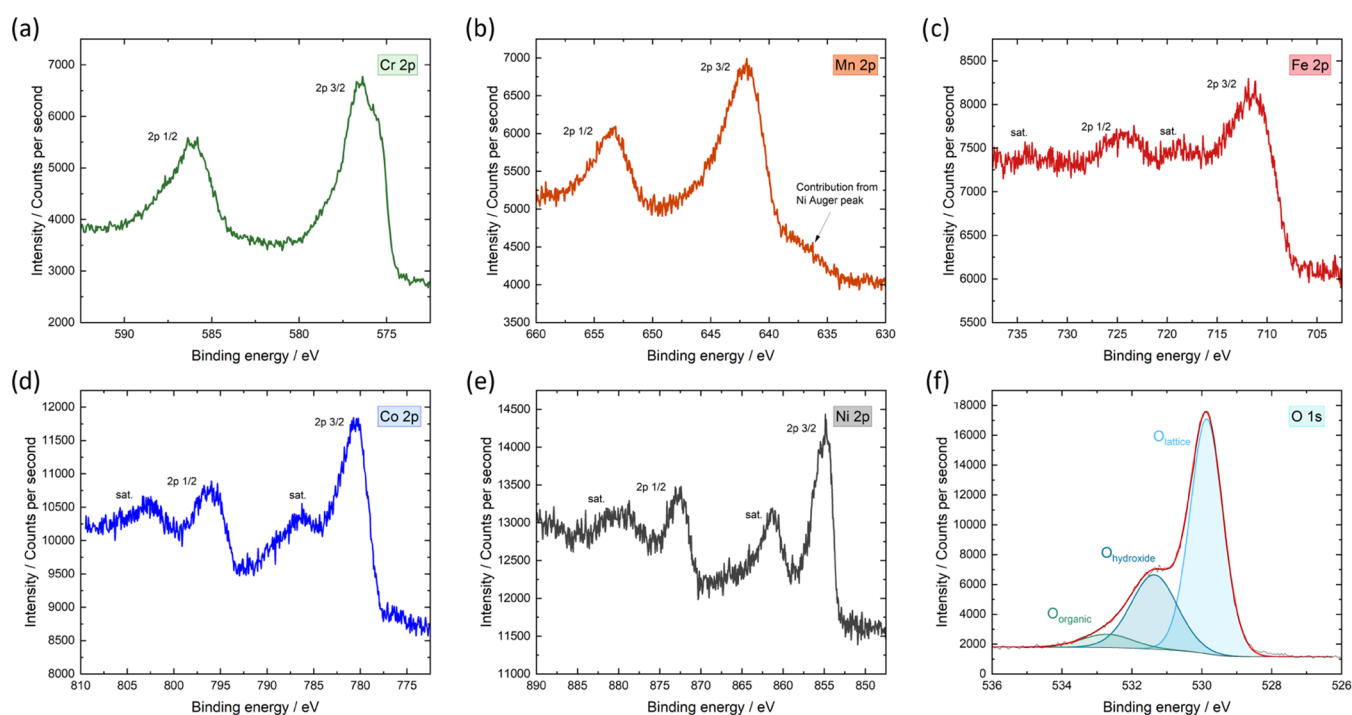
Figure 5. XPS spectra of ML 2-2 MA 155. Panels (a−e) show the 2p spectra of the different metals, and panel (f) shows the 1s spectrum of oxygen.

space of the HEO system. Depositing libraries with all target permutations creates compositional cuts, which are differently located in the composition space (marked with colors in Figure 2b−d), to cover a large compositional range. As the MLs were fabricated, including a Mn−Ni alloy target, the Mn and Ni contents are interdependent. For this reason, Mn and Ni were set in the same direction in the barycentric projection. Each point represents one MA on a ML.

The EDX analysis shows that a composition space of $(Cr_{8−28}Mn_{12−28}Fe_{11−39}Co_{11−37}Ni_{14−31})$-$O_x$ was covered by the three permutations ML 2-1, ML 2-2, and ML 2-3 (Figures 3 and S1, SI).

The XRD crystal structure analysis of all samples obtained at different temperatures and with different sputter target permutations shows a single-phase cubic spinel structure (Fd-3m) for the whole composition space, consistent with the results of previous work.[46−54] Figure 4a,c,e shows five exemplary XRD patterns for each ML permutation (ML 2-1, 2-2, 2-3), assigned to the MAs of the center and closest to the corresponding cathodes. These MAs are highlighted with red squares on the corresponding diffraction angle maps of the most intense peak from the plane (311) (Figure 4b,d,f). Exemplary XRD patterns from the MLs, which were deposited at three different temperatures, can be found in Figure S3, SI. Significant spinel-phase XRD peaks were found for the (111), (220), (311), (222), (400), (422), (511), (440), (620), and (533) planes, whereas the peak for (311) is the most intense.[55] The differences in the XRD patterns in peak intensity and peak position shift are due to differently textured thin-film growth, lattice constants, lattice strains, and composition changes. Compared to nanocrystalline powders of (Co-Cr-Fe-Mn-Ni)$_3$O$_4$,[56] the thin films achieve comparable crystallinity at lower temperatures. The analysis of the reflex position of the (311) plane shows a shift range between a 2θ value of 35.95 and 36.03°, which corresponds to a lattice constant of 0.851 and 0.826 nm, respectively.

XPS analysis was carried out to determine the oxygen content in the spinel thin films. Exemplary XPS spectra for the most active hit composition (ML 2-2 MA 155) are shown in Figure 5. XPS spectra of the most active compositions from ML 2-1 (MA 259) and ML 2-3 (MA 018) can be found in the SI (Figures S5 and S6, for peak positions, see Table S1, SI).[57−63]

The presence of oxygen vacancies can be excluded because the material was not analyzed *in situ*, and it can be assumed that every possible oxygen vacancy was healed by ambient water vapor.[64] For the calculation of the total oxygen content in the material, it is necessary to subtract the carbon-bonded oxygen from the total oxygen. For this purpose, the amount of carbon−oxygen species was determined from the C 1s spectrum (Figure S7, SI).[65] The metal ratios for the most active hit composition were determined from the XPS spectrum as $Cr_{24.6±1.4}Mn_{15.7±2.0}Fe_{16.9±1.8}Co_{26.1±1.9}Ni_{16.6±1.7}$, matching the result from EDX ($Cr_{23}Mn_{16}Fe_{17}Co_{27}Ni_{17}$). The overall oxygen amount without contribution from carbon−oxygen species was 62.2 ± 1.2 atom %. Hence, $(Cr_{24.6±1.4}Mn_{15.7±2.0}Fe_{16.9±1.8}Co_{26.1±1.9}Ni_{16.6±1.7})_{37.8±0.8}O_{62.2±1.2}$ is the most active HEO hit composition with a metal amount error assessed from Gaussian error propagation. Additionally, XPS quantification of MAs along two lines across the MLs, perpendicular to each other (9 MAs per ML), results in an oxygen amount of 62.3 ± 0.6 atom %. The standard deviation of ±0.6 atom % is within the fitting error of the analysis software of 1.2 atom %. The result corresponds well with the expected spinel oxygen amount of 57.1 atom %, derived from the ratio between oxygen and the total number of elements in the spinel-type structure AB$_2$O$_4$,[66] since the total oxygen amount is composed of O$_{lattice}$ from the volume and O$_{hydroxide}$ from the surface.[12,67,68] The normalized oxygen amount for O$_{lattice}$ is 51.8 ± 1.0 atom % with a maximum fitting error of 1.5 atom %. The fact that the measured O$_{lattice}$ amount is lower than the expected oxygen content in the spinel might be the
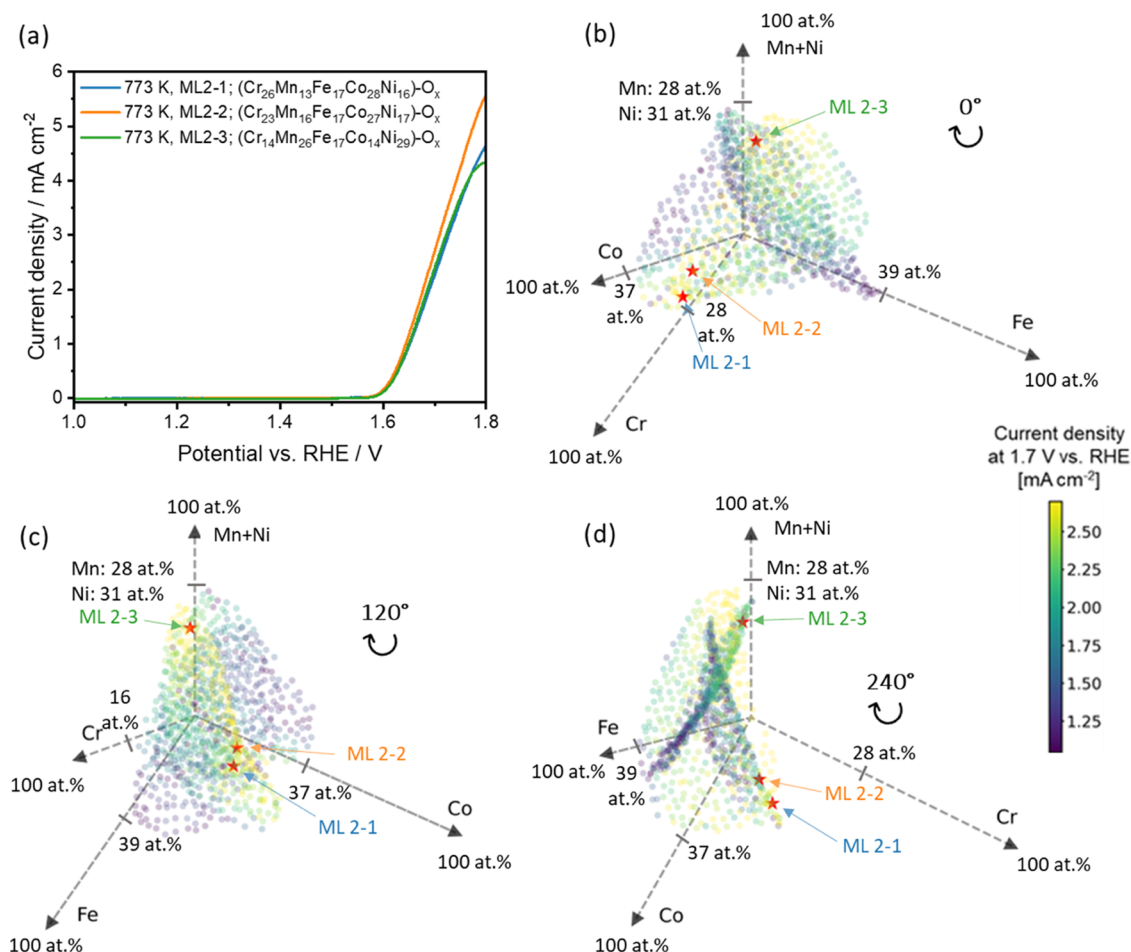
Figure 6. Electrochemical OER activity for the three permutated MLs, which were deposited at 773 K (ML 2-1: blue, 2-2: orange, and 2-3: green). (a) Comparison of the activity of the most active hit composition from each ML. (b−d) Reduced quaternary composition space from different angle perspectives with current density at 1.7 V vs RHE presented as a color map. Most active hit compositions in each permutation are marked with red stars.

result of surface reconstruction under the influence of air moisture, which leads to the transformation of $O_{lattice}$ to $O_{hydroxyde}$, as well as the adsorption of $O_{hydroxyde}$ to the metal atoms. The whole surface composition space of the MLs can be described as $(Cr_{8.1-28.0}Mn_{11.6-28.4}Fe_{10.6-39.0}Co_{11.4-36.7}Ni_{13.5-31.4})_{37.7\pm0.6}O_{62.3\pm0.6}$, with metal ratios from EDX analysis and oxygen amount from XPS analysis.

The low electrical conductivity of most oxide films is a problem for electrochemical applications. The Cantor alloy oxide MLs are not excluded from this, and four-point probe measurements of the thin film (variant A) provide resistance values ranging from 18.1 to 211 MΩ (Figure S8, SI). Furthermore, many of the MAs are beyond the measurement range (>211 MΩ). The results do not show a dependence on composition but on thin film thickness, which is larger in the Mn−Ni cathode direction. Due to the high resistance, OER activity measurements were performed on 50 nm thin films with an underlying electrode layer (variant B), each being a replication of the corresponding 500 nm thin film (A) with identical chemical composition gradients. Significant composition-dependent OER current densities (>0.5 mA cm^{-2} at 1.65 V vs RHE) were recorded on the MLs. The obtained resistance maps of thin film A and electrochemical activity maps of thin film B do not show the same trends, suggesting that the observed activity trends are the result of activity

changes caused by compositional changes and not by changes in sheet resistance due to the film thickness. The resistance of the thin film variant B was not measured with the four-point probe setup because the thickness was too low, and the resistance of the underlying electrode layer would be measured instead.

The electrocatalytic activity toward OER in alkaline electrolytes was evaluated using a high-throughput SDC.[69] Due to the use of the automated setup, the same measurement conditions are maintained for measuring hundreds of MAs, allowing reliable comparison of electrochemical activity data between different MAs and MLs.[39,40,42,70] All measured LSVs, 2D color-coded activity maps, and the comparison of the activity of the most similar compositions prepared at different temperatures as well as the most active hit compositions from different MLs can be found in Figures S11−S13, SI. The electrochemical activity of different MAs is compared using the current density at 1.7 V vs RHE. It is a potential which, at the same time, is high enough to observe significant OER currents and it is also reasonably low to not observe possible limitation of the currents by slow diffusion of reactants. Essentially, the Cantor HEO is a decent OER catalyst in most analyzed compositions. Figure 6 shows the comparison of the electrochemical activity of the permutated MLs. The highest OER activity was obtained for ML 2-2, where compositions
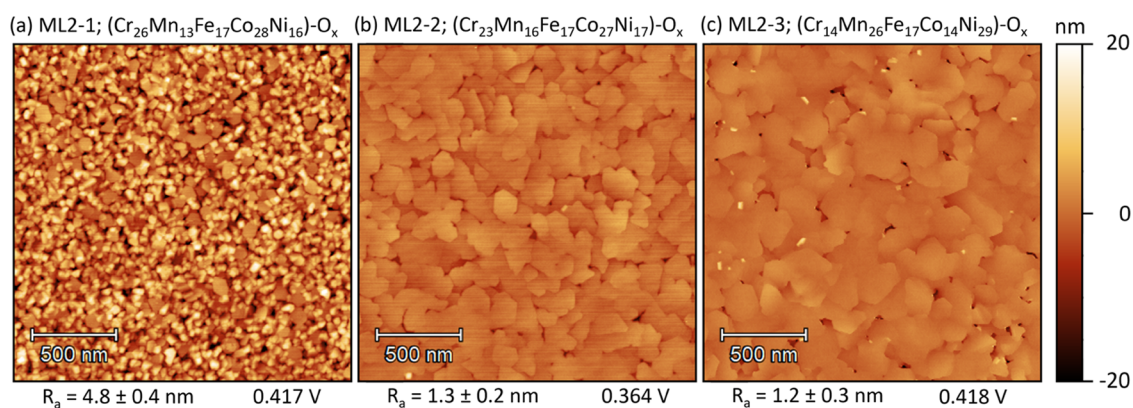
Figure 7. AFM images of the most active compositions from the different permutation depositions at 773 K with the average roughness R_a and the OER overpotential vs RHE at 1 mA cm^{-2}.
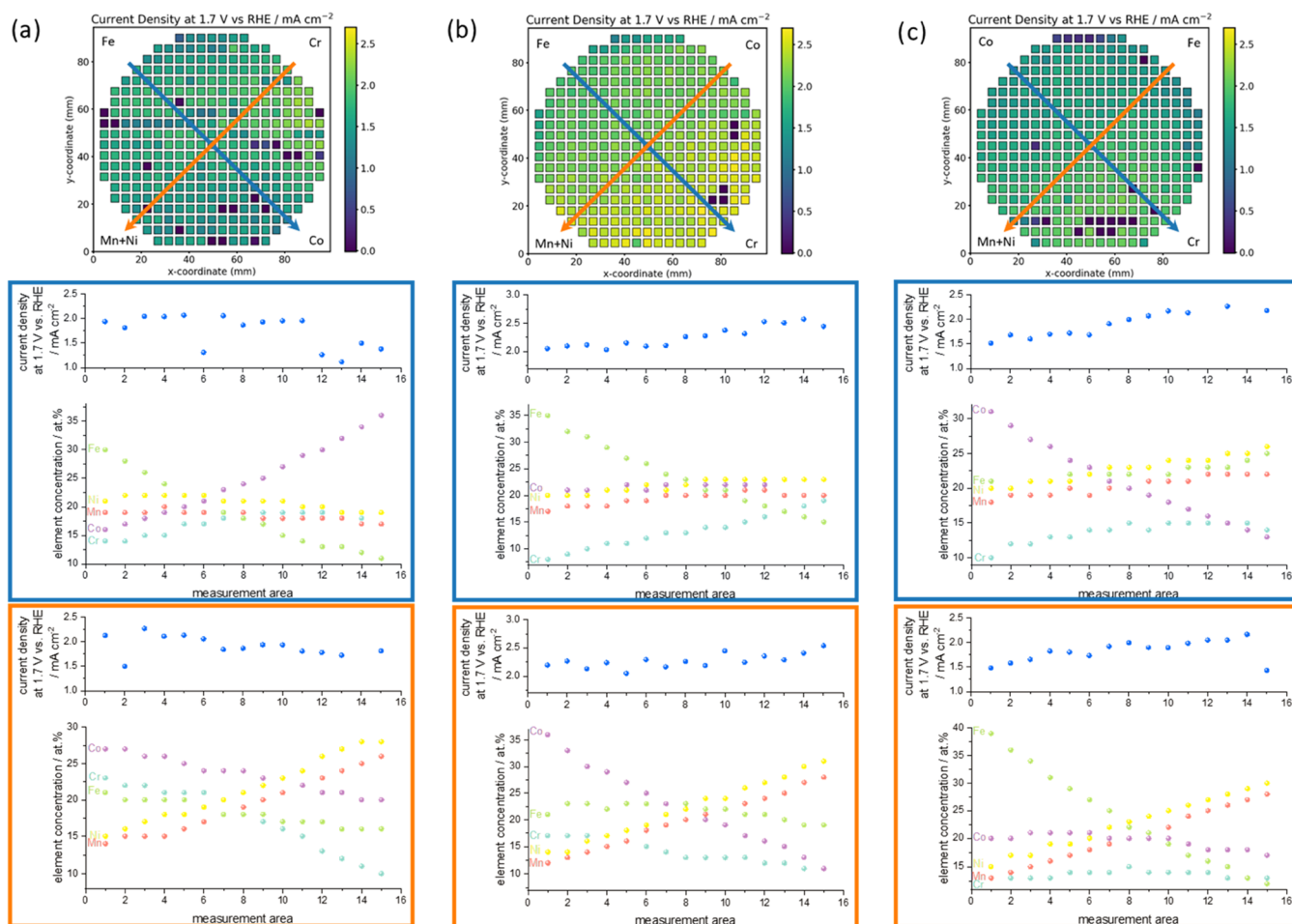

Figure 8. Correlation of the molar ratio of each element (lower plot in the 2nd and 3rd panels) at each of the MAs highlighted with the blue and orange arrows on the color-coded activity maps of MLs (top panel) and the related activity represented by the current at 1.7 V vs RHE (blue dots, upper plot in the 2nd and 3rd panels).

with high Cr, Ni, and Mn content and, at the same time, medium Co content and low Fe content are present. The composition of MA 155 shows the highest current density of 2.69 mA cm^{-2} at 1.7 V vs RHE and the lowest overpotential of 0.36 V at a current density of 1 mA cm^{-2}, which indicates being the most active OER catalyst. Composition was identified by XPS and EDX to be ($Cr_{24.6 \pm 1.4}$-$Mn_{15.7 \pm 2.0}Fe_{16.9 \pm 1.8}Co_{26.1 \pm 1.9}Ni_{16.6 \pm 1.7})_{37.8 \pm 0.8}O_{62.2 \pm 1.2}$ and ($Cr_{23}Mn_{16}Fe_{17}Co_{27}Ni_{17}$)-$O_x$, respectively.

The microstructure and surface morphology of the film, which can vary for different compositions within the same phase, can significantly affect the measured current by changing the geometric surface area and hence the electrochemically active surface. As can be seen in the SEM images, the morphology of the thin films of the MLs prepared at different temperatures changes little between 573 K (ML 1) and 773 K (ML 2-1) but strongly to 973 K (ML 3, Figure S9, SI). ML 3 exhibits the highest surface coarsening, so measured
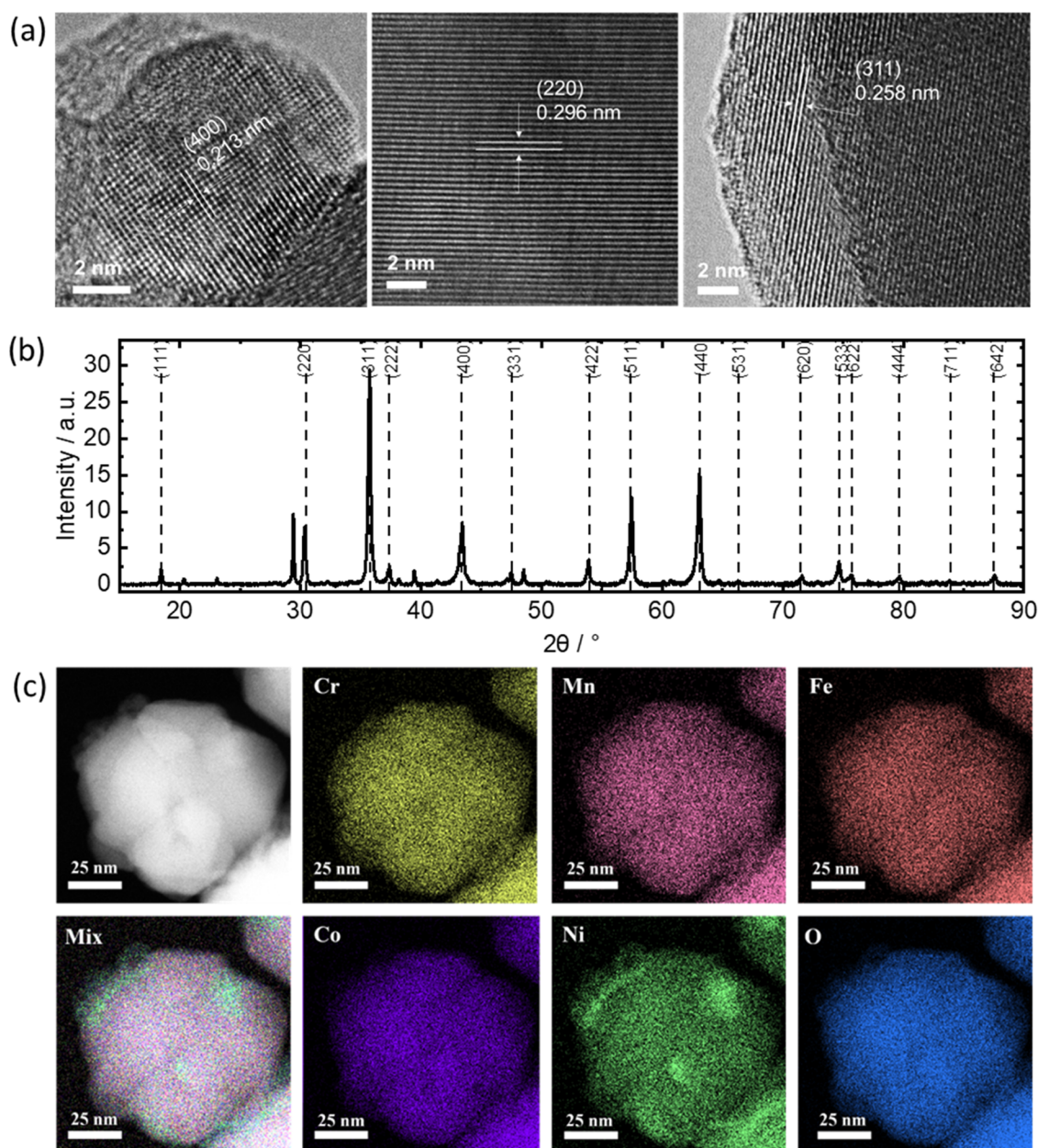
Figure 9. Cantor alloy oxide particles prepared by aerosol synthesis. (a) HR-TEM images with *d* space and respective plane, (b) the XRD pattern with indicated peaks of the spinel phase, and (c) TEM-EDX elemental distribution maps.

currents may increase due to the larger surface area. However, this ML was the least active, suggesting a greater influence of other factors on electrochemical activity than surface morphology. Additionally, SEM investigations revealed no significant changes in sample morphology within one ML. Furthermore, no significant changes in morphology were observed between the permutated MLs (ML 2-1, ML 2-2, or ML 3-3, Figure S10, SI).

Further, AFM measurements of the most active compositions from the permutated MLs show the highest roughness for ML 2-1 (Figure 7a), R_a = 4.8 ± 0.4 nm. The roughness values of ML 2-2 and ML 2-3 are nearly the same (Figure 7b, R_a = 1.3 ± 0.2 and Figure 7c, R_a = 1.2 ± 0.3 nm, respectively). This shows that there is no correlation between surface roughness and electrochemical activity since the most active composition is the hit composition of ML 2-2.

Therefore, we assume that the activity screening in the fabricated MLs is not affected by microstructure effects, i.e., the measured current densities can be interpreted without correction for surface area effects.

To get more insight into the interaction between the electrocatalytic activity and elemental composition of catalysts, we plotted how activity and composition change following the diagonals of the ML for all three permutations (see Figure 8). It seems like electrocatalytic activity increases slightly with decreasing Fe content and increased contents of Cr and Co. This observation might be only used as a hint rather than a fact since from one MA to the next ratios of all elements are changing, i.e., there are no simple linear trends. For example, for permutation 1 (Figure 8a), the blue line from the upper left side to the lower right side follows, at the same time, the direction of the increasing amount of Fe and decreasing amount of Co, with the amounts of Mn, Ni, and Cr kept

relatively constant. This shows the complexity of analyzing activity trends in multi-elemental material systems.

To summarize, the first part of this manuscript describes the characterization of a large fraction of the Cantor alloy oxide system and maps the electrocatalytic activity of all compositions toward the OER to identify the hit composition.

Transfer of the Most Active Hit Composition from Thin-Film Screening to Particles. We used the identified most active hit composition (ML 2-2 MA 155) to synthesize powder-based catalyst particles following a modified aerosol-based synthesis technique as described in the SI (Figure S15) and Cechanaviciute et al.[71] In short, an aerosol of droplets containing the desired composition of individual elements is formed by spraying of the precursor solution onto the deflector plate. Next, aerosol droplets are transported via tubing through the tube furnace, where the solvent evaporates, and dried particles are then collected on the filter paper. Finally, the filter paper was burned away in an oven in a flow of oxygen, and particles were annealed to form the desired spinel oxide structure at 773 K. The synthesized particles were characterized by high-resolution transmission electron microscopy (HR-TEM), EDX, and XRD. Figure 9 shows that the particles are single-phase and crystalline, and the elements are uniformly distributed within the particle. The composition of the spray-synthesized particles was determined to be $(Cr_{23}Mn_{19}Fe_{18}Co_{25}Ni_{15})$-$O_x$ (TEM-EDX line scan of the particle in the SI, Figure S14). The lattice constant calculated from the HR-TEM images for the planes (400), (220), and (311) are 0.852, 0.837, and 0.856 nm, respectively. This corresponds well with the lattice constant of 0.837 nm for the plane (311), calculated from the thin-film XRD pattern of the best-performing composition ML 2-2 MA 155. The TEM analysis revealed that the diameter of the synthesized particles ranges from 75 nm to 1 μm, with the vast majority of 1 μm particles. Even though we obtained particles with different sizes, the elemental distribution and crystallinity are very good and comparable to the measurement error for all particles. These are factors that define the active sites on the surface that determine OER activity. Therefore, the mixture of differently sized particles was used for preparing a modified electrode (see Figures 9 and S14, SI). The XRD analysis of the particles shows spinel oxide and the additional peaks marked in Figure S4, SI can be attributed to $CaCO_3$, which is due to residues of the filter paper used for the collection of the particles.

Catalysts in the form of particles allow the evaluation of electrocatalytic OER activity using standardized methods. Namely, we performed linear sweep voltammetry measurements with a rotating disk electrode (RDE) in 1 M KOH. To do this, a glassy carbon electrode was modified with a catalyst powder suspension comprising Nafion, deionized water, ethanol, and carbon black. The latter which was used to provide sufficient conductivity to the ink. Figure 10 shows the comparison between the LSV measured on a thin film (black) and the LSV of the particle catalyst measured by means of RDE (orange line). Due to the different measurement conditions, such as the diffusion profile, mass transport, etc., resulting from the measurement geometry, electrolyte stirring, and electrolyte concentration, a comparison of current density values in thin-film analysis with SDC and measurement of particles with RDE is not reliable. However, as mentioned before, since OER is a surface reaction either at a thin film or particles, the catalysis should be governed by the adsorption of the species. Thus, an activity comparison at low overpotentials
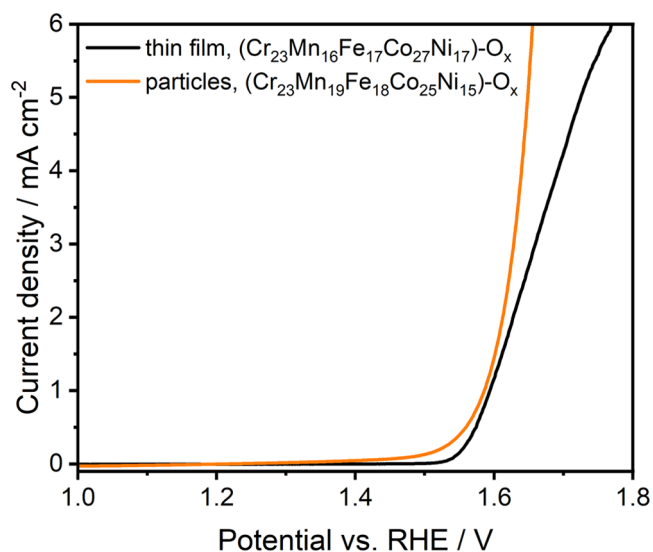
Figure 10. Linear sweep voltammograms (LSV) recorded on a thin film (black) and powder (orange) electrocatalysts show comparable overpotentials for the OER at 1 mA cm^{-2}.

and low current density is possible since the kinetics will dominate the overall reaction. Hence, the overpotential at which currents reach 1 mA cm^{-2} can be reliably compared. The difference in the overpotentials is only 8 mV (thin film: 1.594 V, particles: 1.586 V vs RHE), demonstrating very similar electrocatalytic OER activity. The different slopes of the curves may be caused by the fact that the LSV measured with the RDE setup was iR-corrected, while the data from the high-throughput SDC measurements were not. The high comparability of overpotentials, XRD patterns, elemental composition, and distribution indicates the validity of transferring the thin-film screening results to powder-based electrocatalysts.

CONCLUSIONS

We demonstrated a high-throughput screening of the OER activity of single-phase high-entropy spinel oxides derived from the Cantor alloy and the subsequent transfer of the thin-film hit composition to a powder catalyst. Combinatorial sputter deposition, in combination with a sputter source permutation strategy, covers large parts of the quinary composition space. Single-phase spinel stability across a large composition space was observed. By high-throughput screening, the hit composition $(Cr_{24.6\pm1.4}Mn_{15.7\pm2.0}Fe_{16.9\pm1.8}Co_{26.1\pm1.9}$-$Ni_{16.6\pm1.7})_{37.8\pm0.8}O_{62.2\pm1.2}$ (XPS)/$(Cr_{23}Mn_{16}Fe_{17}Co_{27}Ni_{17})$-$O_x$ (EDX) was identified. This composition was used to synthesize particle-based electrocatalysts. The difference in the overpotential for the OER measured for the thin-film sample and the particles is approximately 8 mV, confirming the successful transfer of the high-throughput screening results to powder catalysts.

ASSOCIATED CONTENT

ⓈSupporting Information

The Supporting Information is available free of charge at https://pubs.acs.org/doi/10.1021/acs.chemmater.2c01455.

Additional characterization figures from EDX, XRD, XPS, resistance, SEM, SDC, and TEM measurements, table including all XPS peak positions, and information

on the determination of the double-layer capacitance of the electrode with particles (PDF)

AUTHOR INFORMATION

Corresponding Author

Alfred Ludwig − *Materials Discovery and Interfaces (MDI), Institute for Materials, Ruhr University Bochum, D-44801 Bochum, Germany; Centre for Interface-Dominated High Performance Materials (ZGH), Ruhr University, Bochum D-44801, Germany;* orcid.org/0000-0003-2802-6774; Email: alfred.ludwig@rub.de

Authors

Valerie Strotkötter − *Materials Discovery and Interfaces (MDI), Institute for Materials, Ruhr University Bochum, D-44801 Bochum, Germany*

Olga A. Krysiak − *Analytical Chemistry − Centre for Electrochemical Sciences (CES), Faculty of Chemistry and Biochemistry, Ruhr University Bochum, D-44801 Bochum, Germany*

Jian Zhang − *Analytical Chemistry − Centre for Electrochemical Sciences (CES), Faculty of Chemistry and Biochemistry, Ruhr University Bochum, D-44801 Bochum, Germany*

Xiao Wang − *Materials Discovery and Interfaces (MDI), Institute for Materials, Ruhr University Bochum, D-44801 Bochum, Germany;* orcid.org/0000-0001-5753-5389

Ellen Suhr − *Materials Discovery and Interfaces (MDI), Institute for Materials, Ruhr University Bochum, D-44801 Bochum, Germany*

Wolfgang Schuhmann − *Analytical Chemistry − Centre for Electrochemical Sciences (CES), Faculty of Chemistry and Biochemistry, Ruhr University Bochum, D-44801 Bochum, Germany;* orcid.org/0000-0003-2916-5223

Complete contact information is available at:
https://pubs.acs.org/10.1021/acs.chemmater.2c01455

Author Contributions

‖V.S. and O.A.K. contributed equally to this paper. V.S. synthesized MLs, conducted high-throughput material characterization of MLs (EDX, XRD, resistance), analyzed and visualized data in Python, and cowrote the original draft. O.A.K.‡ conducted all of the electrochemical measurements (MLs and powder catalyst), analyzed results, synthesized the powder catalysts, and cowrote the original draft. J.Z. conducted HR-TEM, TED-EDX, and STEM imaging. X.W. conducted XPS measurements and supervision of the XPS analysis. E.S. performed SEM high-throughput measurements of the MLs. W.S. and A.L. supervised the electrochemical and materials science part, respectively. All authors reviewed and edited the original draft of the manuscript.

Notes

The authors declare no competing financial interest.

ACKNOWLEDGMENTS

ABBREVIATIONS USED

AFM, atomic force microscopy; EDX, energy-dispersive X-ray spectroscopy; HEA, high-entropy alloy; HEM, high-entropy material; HEO, high-entropy oxide; HR-TEM, high-resolution transmission electron microscopy; LSV, linear sweep voltammogram; MA, measurement area; ML, material library; OER, oxygen reduction reaction; RDE, rotating disk electrode; SDC, scanning droplet cell; SDD, Si drift detector; SEM, scanning electron microscopy; STEM, scanning transmission electron microscopy; XPS, X-ray photoelectron spectroscopy; XRD, X-ray diffraction

REFERENCES

(1) Li, S.; Li, E.; An, X.; Hao, X.; Jiang, Z.; Guan, G. Transition metal-based catalysts for electrochemical water splitting at high current density: current status and perspectives. *Nanoscale* **2021**, *13*, 12788−12817.

(2) Wang, S.; Lu, A.; Zhong, C.-J. Hydrogen production from water electrolysis: role of catalysts. *Nano Convergence* **2021**, *8*, 4.

(3) Shi, Q.; Zhu, C.; Du, D.; Lin, Y. Robust noble metal-based electrocatalysts for oxygen evolution reaction. *Chem. Soc. Rev.* **2019**, *48*, 3181−3192.

(4) Fabbri, E.; Habereder, A.; Waltar, K.; Kötz, R.; Schmidt, T. J. Developments and perspectives of oxide-based catalysts for the oxygen evolution reaction. *Catal. Sci. Technol.* **2014**, *4*, 3800−3821.

(5) Mondschein, J. S.; Callejas, J. F.; Read, C. G.; Chen, J. Y. C.; Holder, C. F.; Badding, C. K.; Schaak, R. E. Crystalline Cobalt Oxide Films for Sustained Electrocatalytic Oxygen Evolution under Strongly Acidic Conditions. *Chem. Mater.* **2017**, *29*, 950−957.

(6) Sun, X.; Xu, K.; Fleischer, C.; Liu, X.; Grandcolas, M.; Strandbakke, R.; Bjørheim, T.; Norby, T.; Chatzitakis, A. Earth-Abundant Electrocatalysts in Proton Exchange Membrane Electrolyzers. *Catalysts* **2018**, *8*, 657.

(7) Huynh, M.; Ozel, T.; Liu, C.; Lau, E. C.; Nocera, D. G. Design of template-stabilized active and earth-abundant oxygen evolution catalysts in acid. *Chem. Sci.* **2017**, *8*, 4779−4794.

(8) Dong, Y.; Komarneni, S. S−trategies to Develop Earth-Abundant Heterogeneous Oxygen Evolution Reaction Catalysts for pH-Neutral or pH-Near-Neutral Electrolytes. *Small Methods* **2021**, *5*, No. e2000719.

(9) Jamesh, M.-I.; Harb, M. Tuning the electronic structure of the earth-abundant electrocatalysts for oxygen evolution reaction (OER) to achieve efficient alkaline water splitting − A review. *J. Energy Chem.* **2021**, *56*, 299−342.

(10) Chen, J. Y. C.; Miller, J. T.; Gerken, J. B.; Stahl, S. S. Inverse spinel NiFeAlO$_4$ as a highly active oxygen evolution electrocatalyst: promotion of activity by a redox-inert metal ion. *Energy Environ. Sci.* **2014**, *7*, 1382.

(11) Ramsundar, R. M.; Pillai, V. K.; Joy, P. A. Spin state engineered Zn$_x$Co$_{3-x}$O$_4$ as an efficient oxygen evolution electrocatalyst. *Phys. Chem. Chem. Phys.* **2018**, *20*, 29452−29461.

(12) Zhou, Y.; Sun, S.; Wei, C.; Sun, Y.; Xi, P.; Feng, Z.; Xu, Z. J. Significance of Engineering the Octahedral Units to Promote the Oxygen Evolution Reaction of Spinel Oxides. *Adv. Mater.* **2019**, *31*, No. e1902509.

(13) Cui, M.; Ding, X.; Huang, X.; Shen, Z.; Lee, T.-L.; Oropeza, F. E.; Hofmann, J. P.; Hensen, E. J. M.; Zhang, K. H. L. Ni^{3+}-Induced Hole States Enhance the Oxygen Evolution Reaction Activity of Ni$_x$Co$_{3-x}$O$_4$ Electrocatalysts. *Chem. Mater.* **2019**, *31*, 7618−7625.

(14) Gao, Y.; Liu, Y.; Yu, H.; Zou, D. High-entropy oxides for catalysis: Status and perspectives. *Appl. Catal., A* **2022**, *631*, No. 118478.

(15) Oses, C.; Toher, C.; Curtarolo, S. High-entropy ceramics. *Nat Rev Mater* **2020**, *5*, 295−309.

(16) Amiri, A.; Shahbazian-Yassar, R. Recent progress of high-entropy materials for energy storage and conversion. *J. Mater. Chem. A* **2021**, *9*, 782−823.

(17) Fu, M.; Ma, X.; Zhao, K.; Li, X.; Su, D. High-entropy materials for energy-related applications. *iScience* **2021**, *24*, No. 102177.

(18) Löffler, T.; Meyer, H.; Savan, A.; Wilde, P.; Garzón Manjón, A.; Chen, Y.-T.; Ventosa, E.; Scheu, C.; Ludwig, A.; Schuhmann, W. Discovery of a Multinary Noble Metal-Free Oxygen Reduction Catalyst. *Adv. Energy Mater.* **2018**, *8*, No. 1802269.

(19) Löffler, T.; Savan, A.; Meyer, H.; Meischein, M.; Strotkötter, V.; Ludwig, A.; Schuhmann, W. Design of Complex Solid-Solution Electrocatalysts by Correlating Configuration, Adsorption Energy Distribution Patterns, and Activity Curves. *Angew. Chem., Int. Ed.* **2020**, *59*, 5844−5850.

(20) Batchelor, T. A.; Pedersen, J. K.; Winther, S. H.; Castelli, I. E.; Jacobsen, K. W.; Rossmeisl, J. High-Entropy Alloys as a Discovery Platform for Electrocatalysis. *Joule* **2019**, *3*, 834−845.

(21) Yao, Y.; Huang, Z.; Xie, P.; Lacey, S. D.; Jacob, R. J.; Xie, H.; Chen, F.; Nie, A.; Pu, T.; Rehwoldt, M.; Yu, D.; Zachariah, M. R.; Wang, C.; Shahbazian-Yassar, R.; Li, J.; Hu, L. Carbothermal shock synthesis of high-entropy-alloy nanoparticles. *Science* **2018**, *359*, 1489−1494.

(22) Sun, Y.; Dai, S. High-entropy materials for catalysis: A new frontier. *Sci. Adv.* **2021**, *7*, No. eabg1600.

(23) Cantor, B.; Chang, I.; Knight, P.; Vincent, A. Microstructural development in equiatomic multicomponent alloys. *Mater. Sci. Eng., A* **2004**, *375−377*, 213−218.

(24) Yeh, J.-W.; Chen, S.-K.; Lin, S.-J.; Gan, J.-Y.; Chin, T.-S.; Shun, T.-T.; Tsau, C.-H.; Chang, S.-Y. Nanostructured High-Entropy Alloys with Multiple Principal Elements: Novel Alloy Design Concepts and Outcomes. *Adv. Eng. Mater.* **2004**, *6*, 299−303.

(25) Rost, C. M.; Sachet, E.; Borman, T.; Moballegh, A.; Dickey, E. C.; Hou, D.; Jones, J. L.; Curtarolo, S.; Maria, J.-P. Entropy-stabilized oxides. *Nat. Commun.* **2015**, *6*, No. 8485.

(26) Liu, C.; Zhu, H.; Lu, S.; Duan, F.; Du, M. High entropy alloy nitrides with integrated nanowire/nanosheet architecture for efficient alkaline hydrogen evolution reactions. *New J. Chem.* **2021**, *45*, 22255−22260.

(27) Jin, T.; Sang, X.; Unocic, R. R.; Kinch, R. T.; Liu, X.; Hu, J.; Liu, H.; Dai, S. Mechanochemical-Assisted Synthesis of High-Entropy Metal Nitride via a Soft Urea Strategy. *Adv. Mater* **2018**, *30*, No. e1707512.

(28) Zhao, X.; Xue, Z.; Chen, W.; Wang, Y.; Mu, T. Eutectic Synthesis of High-Entropy Metal Phosphides for Electrocatalytic Water Splitting. *ChemSusChem* **2020**, *13*, 2038−2042.

(29) Zhou, J.; Zhang, J.; Zhang, F.; Niu, B.; Lei, L.; Wang, W. High-entropy carbide: A novel class of multicomponent ceramics. *Ceramics Int.* **2018**, *44*, 22014−22018.

(30) Sukkurji, P. A.; Cui, Y.; Lee, S.; Wang, K.; Azmi, R.; Sarkar, A.; Indris, S.; Bhattacharya, S. S.; Kruk, R.; Hahn, H.; Wang, Q.; Botros, M.; Breitung, B. Mechanochemical synthesis of novel rutile-type high entropy fluorides for electrocatalysis. *J. Mater. Chem. A* **2021**, *9*, 8998−9009.

(31) Wang, T.; Chen, H.; Yang, Z.; Liang, J.; Dai, S. High-Entropy Perovskite Fluorides: A New Platform for Oxygen Evolution Catalysis. *J. Am. Chem. Soc.* **2020**, *142*, 4550−4554.

(32) Cui, M.; Yang, C.; Li, B.; Dong, Q.; Wu, M.; Hwang, S.; Xie, H.; Wang, X.; Wang, G.; Hu, L. High-Entropy Metal Sulfide Nanoparticles Promise High-Performance Oxygen Evolution Reaction. *Adv. Energy Mater.* **2021**, *11*, No. 2002887.

(33) Nguyen, T. X.; Su, Y.-H.; Lin, C.-C.; Ting, J.-M. Self-Reconstruction of Sulfate-Containing High Entropy Sulfide for Exceptionally High-Performance Oxygen Evolution Reaction Electrocatalyst. *Adv. Funct. Mater.* **2021**, *31*, No. 2106229.

(34) Zhang, Y.; Jiang, Z.-B.; Sun, S.-K.; Guo, W.-M.; Chen, Q.-S.; Qiu, J.-X.; Plucknett, K.; Lin, H.-T. Microstructure and mechanical properties of high-entropy borides derived from boro/carbothermal reduction. *J. Eur. Ceram. Soc.* **2019**, *39*, 3920−3924.

(35) Zuo, Y.; Rao, D.; Ma, S.; Li, T.; Tsang, Y. H.; Kment, S.; Chai, Y. Valence Engineering via Dual-Cation and Boron Doping in Pyrite Selenide for Highly Efficient Oxygen Evolution. *ACS Nano* **2019**, *13*, 11469−11476.

(36) Qin, Y.; Liu, J.-X.; Li, F.; Wei, X.; Wu, H.; Zhang, G.-J. A high entropy silicide by reactive spark plasma sintering. *J Adv. Ceram.* **2019**, *8*, 148−152.

(37) Zhang, L.; Cai, W.; Bao, N. Top-Level Design Strategy to Construct an Advanced High-Entropy Co-Cu-Fe-Mo (Oxy)-Hydroxide Electrocatalyst for the Oxygen Evolution Reaction. *Adv. Mater.* **2021**, *33*, No. e2100745.

(38) Zhao, X.; Xue, Z.; Chen, W.; Bai, X.; Shi, R.; Mu, T. Ambient fast, large-scale synthesis of entropy-stabilized metal−organic framework nanosheets for electrocatalytic oxygen evolution. *J. Mater. Chem. A* **2019**, *7*, 26238−26242.

(39) Batchelor, T. A. A.; Löffler, T.; Xiao, B.; Krysiak, O. A.; Strotkötter, V.; Pedersen, J. K.; Clausen, C. M.; Savan, A.; Li, Y.; Schuhmann, W.; Rossmeisl, J.; Ludwig, A. Complex-Solid-Solution Electrocatalyst Discovery by Computational Prediction and High-Throughput Experimentation. *Angew. Chem., Int. Ed.* **2021**, *60*, 6932−6937.

(40) Krysiak, O. A.; Schumacher, S.; Savan, A.; Schuhmann, W.; Ludwig, A.; Andronescu, C. Searching novel complex solid solution electrocatalysts in unconventional element combinations. *Nano Res.* **2022**, *15*, 4780−4784.

(41) Schumacher, S.; Baha, S.; Savan, A.; Andronescu, C.; Ludwig, A. High-throughput discovery of hydrogen evolution electrocatalysts in the complex solid solution system Co−Cr−Fe−Mo−Ni. *J. Mater. Chem. A* **2022**, *10*, 9981−9987.

(42) Banko, L.; Krysiak, O. A.; Pedersen, J. K.; Xiao, B.; Savan, A.; Löffler, T.; Baha, S.; Rossmeisl, J.; Schuhmann, W.; Ludwig, A. Unravelling Composition−Activity−Stability Trends in High Entropy Alloy Electrocatalysts by Using a Data-Guided Combinatorial Synthesis Strategy and Computational Modeling. *Adv. Energy Mater.* **2022**, *12*, No. 2103312.

(43) Ludwig, A. Discovery of new materials using combinatorial synthesis and high-throughput characterization of thin-film materials libraries combined with computational methods. *npj Comput Mater* **2019**, *5*, No. 70.

(44) Pedersen, J. K.; Clausen, C. M.; Krysiak, O. A.; Xiao, B.; Batchelor, T. A. A.; Löffler, T.; Mints, V. A.; Banko, L.; Arenz, M.; Savan, A.; Schuhmann, W.; Ludwig, A.; Rossmeisl, J. Bayesian Optimization of High-Entropy Alloy Compositions for Electro-catalytic Oxygen Reduction. *Angew. Chem., Int. Ed.* **2021**, *60*, 24144−24152.

(45) Löffler, T.; Ludwig, A.; Rossmeisl, J.; Schuhmann, W. What Makes High-Entropy Alloys Exceptional Electrocatalysts? *Angew. Chem., Int. Ed.* **2021**, *60*, 26894−26903.

(46) Dąbrowa, J.; Stygar, M.; Mikuła, A.; Knapik, A.; Mroczka, K.; Tejchman, W.; Danielewski, M.; Martin, M. Synthesis and micro-structure of the $(Co,Cr,Fe,Mn,Ni)_3O_4$ high entropy oxide charac-terized by spinel structure. *Mater. Lett.* **2018**, *216*, 32−36.

(47) Einert, M.; Mellin, M.; Bahadorani, N.; Dietz, C.; Lauterbach, S.; Hofmann, J. P. Mesoporous High-Entropy Oxide Thin Films: Electrocatalytic Water Oxidation on High-Surface-Area Spine $(Cr_{0.2}Mn_{0.2}Fe_{0.2}Co_{0.2}Ni_{0.2})_3O_4$ Electrodes. *ACS Appl. Energy Mater.* **2022**, *5*, 717−730.

(48) Sun, Z.; Zhao, Y.; Sun, C.; Ni, Q.; Wang, C.; Jin, H. High entropy spinel-structure oxide for electrochemical application. *Chem. Eng. J.* **2022**, *431*, No. 133448.

(49) Wei, J.; Rong, K.; Li, X.; Wang, Y.; Qiao, Z.-A.; Fang, Y.; Dong, S. Deep eutectic solvent assisted facile synthesis of low-dimensional hierarchical porous high-entropy oxides. *Nano Res.* **2022**, *15*, 2756−2763.

(50) Minouei, H.; Kheradmandfard, M.; Saboktakin Rizi, M.; Jalaly, M.; Kim, D.-E.; Ig Hong, S. Formation Mechanism of High-Entropy Spinel Thin Film and its Mechanical and Magnetic Properties: Linking High-Entropy Alloy to High-Entropy Ceramic. *Appl. Surf. Sci.* **2021**, *576*, No. 151719.

(51) Talluri, B.; Aparna, M. L.; Sreenivasulu, N.; Bhattacharya, S. S.; Thomas, T. High entropy spinel metal oxide $(CoCrFeMnNi)_3O_4$ nanoparticles as a high-performance supercapacitor electrode material. *J. Energy Storage* **2021**, *42*, No. 103004.

(52) Grzesik, Z.; Smoła, G.; Miszczak, M.; Stygar, M.; Dąbrowa, J.; Zajusz, M.; Swierczek, K.; Danielewski, M. Defect structure and transport properties of $(Co,Cr,Fe,Mn,Ni)_3O_4$ spinel-structured high entropy oxide. *J. Eur. Ceram. Soc.* **2020**, *40*, 835–839.

(53) Sarkar, A.; Eggert, B.; Witte, R.; Lill, J.; Velasco, L.; Wang, Q.; Sonar, J.; Ollefs, K.; Bhattacharya, S. S.; Brand, R. A.; Wende, H.; Groot, F. M.; de Clemens, O.; Hahn, H.; Kruk, R. Comprehensive investigation of crystallographic, spin-electronic and magnetic structure of $(Co_{0.2}Cr_{0.2}Fe_{0.2}Mn_{0.2}Ni_{0.2})_3O_4$: Unraveling the suppression of configuration entropy in high entropy oxides. *Acta Mater.* **2022**, *226*, No. 117581.

(54) Musicó, B.; Wright, Q.; Ward, T. Z.; Grutter, A.; Arenholz, E.; Gilbert, D.; Mandrus, D.; Keppens, V. Tunable magnetic ordering through cation selection in entropic spinel oxides. *Phys. Rev. Mater.* **2019**, *3*, No. 104416.

(55) Wang, D.; Jiang, S.; Duan, C.; Mao, J.; Dong, Y.; Dong, K.; Wang, Z.; Luo, S.; Liu, Y.; Qi, X. Spinel-structured high entropy oxide $(FeCoNiCrMn)_3O_4$ as anode towards superior lithium storage performance. *J. Alloys Compd.* **2020**, *844*, No. 156158.

(56) Mao, A.; Quan, F.; Xiang, H.-Z.; Zhang, Z.-G.; Kuramoto, K.; Xia, A.-L. Facile synthesis and ferrimagnetic property of spinel $(CoCrFeMnNi)_3O_4$ high-entropy oxide nanocrystalline powder. *J. Mol. Struct.* **2019**, *1194*, 11–18.

(57) Biesinger, M. C.; Payne, B. P.; Grosvenor, A. P.; Lau, L. W.; Gerson, A. R.; Smart, R. S. Resolving surface chemical states in XPS analysis of first row transition metals, oxides and hydroxides: Cr, Mn, Fe, Co and Ni. *Appl. Surf. Sci.* **2011**, *257*, 2717–2730.

(58) Minouei, H.; Kheradmandfard, M.; Saboktakin Rizi, M.; Jalaly, M.; Kim, D.-E.; Hong, S. I. Formation mechanism of high-entropy spinel thin film and its mechanical and magnetic properties: Linking high-entropy alloy to high-entropy ceramic. *Appl. Surf. Sci.* **2022**, *576*, No. 151719.

(59) Chen, Z.; Wang, J.; Chao, D.; Baikie, T.; Bai, L.; Chen, S.; Zhao, Y.; Sum, T. C.; Lin, J.; Shen, Z. Hierarchical Porous $LiNi_{1/3}Co_{1/3}Mn_{1/3}O_2$ Nano-/Micro Spherical Cathode Material: Minimized Cation Mixing and Improved Li^+ Mobility for Enhanced Electrochemical Performance. *Sci. Rep.* **2016**, *6*, No. 25771.

(60) Wang, L.; Mercier, D.; Zanna, S.; Seyeux, A.; Laurent-Brocq, M.; Perrière, L.; Guillot, I.; Marcus, P. Study of the surface oxides and corrosion behaviour of an equiatomic CoCrFeMnNi high entropy alloy by XPS and ToF-SIMS. *Corros. Sci.* **2020**, *167*, No. 108507.

(61) Koo, C.; Hong, H.; Im, P. W.; Kim, H.; Lee, C.; Jin, X.; Yan, B.; Lee, W.; Im, H.-J.; Paek, S. H.; Piao, Y. Magnetic and near-infrared derived heating characteristics of dimercaptosuccinic acid coated uniform $Fe@Fe_3O_4$ core-shell nanoparticles. *Nano Convergence* **2020**, *7*, No. 20.

(62) Anantharamaiah, P. N.; Joy, P. A. Enhancing the strain sensitivity of $CoFe_2O_4$ at low magnetic fields without affecting the magnetostriction coefficient by substitution of small amounts of Mg for Fe. *Phys. Chem. Chem. Phys.* **2016**, *18*, 10516–10527.

(63) Nguyen, T. X.; Patra, J.; Chang, J.-K.; Ting, J.-M. High entropy spinel oxide nanoparticles for superior lithiation–delithiation performance. *J. Mater. Chem. A* **2020**, *8*, 18963–18973.

(64) Idriss, H. On the wrong assignment of the XPS O1s signal at 531–532 eV attributed to oxygen vacancies in photo- and electro-catalysts for water splitting and other materials applications. *Surf. Sci.* **2021**, *712*, No. 121894.

(65) Payne, B. P.; Biesinger, M. C.; McIntyre, N. S. X-ray photoelectron spectroscopy studies of reactions on chromium metal and chromium oxide surfaces. *J. Electron Spectrosc. Relat. Phenom.* **2011**, *184*, 29–37.

(66) West, A. R. *Solid State Chemistry and Its Applications*, 2nd ed.; Wiley, 2022.

(67) Busca, G.; Lorenzelli, V.; Ramis, G.; Willey, R. J. Surface sites on spinel-type and corundum-type metal oxide powders. *Langmuir* **1993**, *9*, 1492–1499.

(68) Duan, Y.; Sun, S.; Sun, Y.; Xi, S.; Chi, X.; Zhang, Q.; Ren, X.; Wang, J.; Ong, S. J. H.; Du, Y.; Gu, L.; Grimaud, A.; Xu, Z. J. Mastering Surface Reconstruction of Metastable Spinel Oxides for Better Water Oxidation. *Adv. Mater.* **2019**, *31*, No. e1807898.

(69) Sliozberg, K.; Schäfer, D.; Erichsen, T.; Meyer, R.; Khare, C.; Ludwig, A.; Schuhmann, W. High-throughput screening of thin-film semiconductor material libraries I: system development and case study for Ti-W-O. *ChemSusChem* **2015**, *8*, 1270–1278.

(70) Krysiak, O. A.; Junqueira, J. R. C.; Conzuelo, F.; Bobrowski, T.; Wilde, P.; Wysmolek, A.; Schuhmann, W. Tuning Light-Driven Water Oxidation Efficiency of Molybdenum-Doped $BiVO_4$ by Means of Multicomposite Catalysts Containing Nickel, Iron, and Chromium Oxides. *ChemPlusChem* **2020**, *85*, 327–333.

(71) Cechanaviciute, I. A.; Bobrowski, T.; Jambrec, D.; Krysiak, O. A.; Brix, A. C.; Braun, M.; Quast, T.; Wilde, P.; Morales, D. M.; Andronescu, C.; Schuhmann, W. Aerosol-Based Synthesis of Multimetal Electrocatalysts for Oxygen Evolution and Glycerol Oxidation. *ChemElectroChem* **2022**, *9*, No. e202200107.